Changes in Iris Stiffness and Permeability in Primary Angle Closure Glaucoma

Satish K. Panda,[1,2] Royston K. Y. Tan,[1,2] Tin A. Tun,[3] Martin L. Buist,[2] Monisha Nongpiur,[3] Mani Baskaran,[3,4] Tin Aung,[3,5,6] and Michaël J. A. Girard[1,5,7]

[1]Ophthalmic Engineering & Innovation Laboratory (OEIL), Singapore Eye Research Institute, Singapore National Eye Centre, Singapore
[2]Department of Biomedical Engineering, National University of Singapore, Singapore
[3]Singapore Eye Research Institute, Singapore National Eye Centre, Singapore
[4]Sankara Nethralaya, Chennai, India
[5]Duke-NUS Medical School, Singapore
[6]Department of Ophthalmology, Yong Loo Lin School of Medicine, National University of Singapore, Singapore
[7]Institute of Molecular & Clinical Ophthalmology, Basel, Switzerland

Correspondence: Michaël J. A. Girard, Ophthalmic Engineering and Innovation Laboratory, Singapore Eye Research Institute, 20 College Road Discovery Tower, The Academia 169856, Singapore; mgirard@ophthalmic.engineering.

Received: May 30, 2021
Accepted: September 30, 2021
Published: October 29, 2021

Citation: Panda SK, Tan RKY, Tun TA, et al. Changes in iris stiffness and permeability in primary angle closure glaucoma. *Invest Ophthalmol Vis Sci*. 2021;62(13):29. https://doi.org/10.1167/iovs.62.13.29

Purpose. To evaluate the biomechanical properties of the iris by evaluating iris movement during pupil constriction and to compare such properties between healthy and primary angle-closure glaucoma (PACG) subjects.

Methods. A total of 140 subjects were recruited for this study. In a dark room, the anterior segments of one eye per subject were scanned using anterior segment optical coherence tomography imaging during induced pupil constriction with an external white light source of 1700 lux. Using a custom segmentation code, we automatically isolated the iris segments from the AS-OCT images, which were then discretized and transformed into a three-dimensional point cloud. For each iris, a finite element (FE) mesh was constructed from the point cloud, and an inverse FE simulation was performed to match the clinically observed iris constriction in the AS-OCT images. Through this optimization process, we were able to identify the elastic modulus and permeability of each iris.

Results. For all 140 subjects (95 healthy and 45 PACG of Indian/Chinese ethnicity; age 60.2 ± 8.7 for PACG subjects and 57.7 ± 10.1 for healthy subjects), the simulated deformation pattern of the iris during pupil constriction matched well with OCT images. We found that the iris stiffness was higher in PACG than in healthy controls (24.5 ± 8.4 kPa vs. 17.1 ± 6.6 kPa with 40 kPa of active stress specified in the sphincter region; $P < 0.001$), whereas iris permeability was lower (0.41 ± 0.2 mm^2/kPa s vs. 0.55 ± 0.2 mm^2/kPa s; $p = 0.142$).

Conclusions. This study suggests that the biomechanical properties of the iris in PACG are different from those in healthy controls. An improved understanding of the biomechanical behavior of the iris may have implications for the understanding and management of angle-closure glaucoma.

Keywords: primary angle closure glaucoma, iris biomechanics, finite element method, iris permeability

Primary angle-closure glaucoma (PACG) causes irreversible blindness and affects four million people worldwide.[1] A narrower anterior chamber angle is the main predisposing characteristic of eyes with PACG.[2,3] Several anatomical features, such as a shallow anterior chamber depth, a short axial length, and a small anterior chamber width, are the other major PACG risk factors.[4] However, several studies have reported that only a small proportion of those with narrow angles or with other PACG risk factors develop PACG.[5,6] In the study by Friedman et al.,[7] PACG eyes responded differently to changes in illumination compared to healthy eyes with the same level of narrow angles. This suggests that a static morphologic assessment of the anterior chamber may not be sufficient PACG diagnosis, and instead, dynamic physiological changes of ocular structures (such as iris movement during miosis/mydriasis) could prove pertinent.

Several studies have reported associations between iris biomechanics and PACG. For instance, the density of collagen fibers in the iris is higher in PACG than in healthy subjects as characterized through histology.[4] Narayanaswamy et al.[8] performed biomechanical testing on excised iris strips and found that PACG eyes exhibited a higher iris stiffness compared to healthy eyes. However, characterizing the stiffness of the iris in an ex vivo setting has poor clinical applicability because it requires an invasive procedure to harvest a large biopsy specimen. Because of this limitation, Pant et al.[9] proposed a noninvasive in

vivo procedure to evaluate iris stiffness directly from optical coherence tomography (OCT) images. Although this was an important piece of work, it was limited by the assumption that the iris was a hyperelastic solid that could not exchange water with the anterior chamber. Because of this limitation, the reported stiffness values may not reflect the true tissue properties.

From a biomechanical point of view, the iris is composed of two phases, a solid phase and a fluid phase.[10] It contains a large amount of water that can easily flow in and out during miosis or mydriasis. The ability of the iris to absorb or exude fluid is defined by its permeability, with a high permeability allowing more water movement across the iris. This water movement can affect the entire volume of the iris. For instance, several studies have shown that the volume of the iris can change during pupillary constriction/dilation.[11] In addition, iris surface features, known as crypts and furrows, were found to be correlated with the rate of volume change.[11–13] It has also been reported that eyes with thicker and larger irides (i.e., a larger iris volume) are more prone to angle-closure.[14] Thus, measuring the permeability of the iris in vivo (in addition to its stiffness) may provide useful information about its pathophysiological states.

In this study, we aimed to evaluate the stiffness and permeability of the iris during pupil constriction using an inverse finite element (FE) approach in both PACG and age-matched healthy subjects. We considered the iris to be a heterogeneous structure with a permeable stroma layer and modeled it as a biphasic material thus allowing for water movement.

Methods

Patient Recruitment and Imaging

A total of 140 subjects (95 healthy and 45 PACG) were recruited for this study at the Singapore Eye Research Institute, Singapore. Written informed consent was obtained for all patients. The study was conducted following the tenets of the World Medical Associations Declaration of Helsinki and had ethics approval from the SingHealth Centralized Institutional Review Board. PACG was defined as an eye with occludable angles (the pigmented posterior trabecular meshwork was not seen on non-indentation gonioscopy for at least 180° in the primary glaze position) and glaucomatous optic neuropathy was defined as the presence of vertical cup-disc ratio >0.8 or neuroretinal rim thinning with an associated visual field loss that was repeatable on two separate occasions on standard automated perimetry. All subjects underwent anterior segment imaging using swept-source OCT imaging (SS-1000 CASIA; Tomey Corporation, Nagoya, Japan) in the primary gaze position before any contact procedures. OCT imaging was performed with the "angle analysis" protocol (video mode) to obtain "live" horizontal B-Scans of the anterior segment (0° to 180°, limbal to limbal), and the acquisition time was 0.125 second per line, that is, eight frames per second. The recording of the OCT video was started one minute after dark adaption using a standard protocol (light intensity was approximately 20 lux as measured by Studio Deluxe II L-398, Sekonic, Japan). A torchlight flashed the fellow eye from the temporal side 15° off-axis (approximately 1700 lux).[15] Changes in the anterior chamber and iris from dark to light were acquired. If motion artifacts were observed, the procedure was repeated up to a maximum of three times to prevent iris muscle fatigue. Each frame was 16 mm in length and 6 mm in depth.

Segmentation of OCT Images and 3D Reconstruction

We extracted 10 frames from the OCT video of each subject such that the complete iris movement, from its initial fully-dilated position to its deformed position (fully-constricted), could be observed. The iris roots (IR) on both sides were identified in each frame, and the images were rotated in such a way that both IRs were aligned horizontally (see Figs. 1a, 1b). Using a custom Python code, we delineated the left and right iris cross-sectional boundaries in each of the ten frames manually and discretized them into a set of points (Figs. 1c–1e).

We assumed the iris to be a rotationally symmetric structure around an anteroposterior geometric axis (APGA). The midpoint of the line segment joining both IRs was considered the origin, and the bisecting perpendicular line was treated as the APGA (Fig. 1b). The boundary points on the left cross-section of the iris were then rotated by 180° about the APGA to create a three-dimensional (3D) point cloud (Fig. 1f). During the rotation, the points on the left face were transformed in such a way that the shape of the left iris would transform into that of the right after the rotation. Using a custom Python code, at first, we generated a node connectivity matrix and a 3D mesh for the iris, consisting of 4600 eight-node trilinear hexahedral elements and the different tissue layers (i.e., stroma, iris pigment epithelial layer [PEL], and sphincter layer) were then identified in the mesh (Figs. 1g, 1h). The mesh density was based on a preliminary convergence study.

The anterior-boundary-layer of the iris was considered to be a part of the stroma because it was thought to be unlikely to provide any significant mechanical resistance during deformation. Similarly, the dilator region was not specified because our study primarily focused on pupil constriction but not dilation. The PEL is a single-cell layer on the posterior side of the iris that restricts the movement of water. We thus created a thin PEL in our mesh to prevent any fluid movement from the posterior side. During miosis/mydriasis, the iris tip slides over the lens surface. We therefore digitized the boundary of the lens in the OCT image and meshed it with 4-noded linear quadrilateral shell elements (Figs. 1d, 1g). For simplicity, the lens was treated as a nondeformable material (also known as rigid body), over which the iris could slide during constriction.

The morphometric measurements of the iris, as reported in numerous literatures, reveal that the average thickness and length of the sphincter from the pupillary margin are 0.134 ± 0.02 mm and 2.45 ± 0.14 mm, respectively, whereas the average thickness of the iris is 0.735 ± 0.02 mm.[16,17] In our FE models, the sphincter was scaled with the thickness of the iris so as to maintain the same iris to sphincter thickness ratio (Figs. 1i, 1j). Figure 1j shows one of our FE mesh with the corresponding dimensions for the sphincter muscle and the iris. The location of the sphincter muscle cannot be identified from the AS-OCT images. Its location was based on histological observations and one that would allow realistic motion during constriction. Of note, a sphincter that is either too anteriorly or posteriorly located would result in abnormal iris motion as observed in Figure 5.

Investigative Ophthalmology & Visual Science

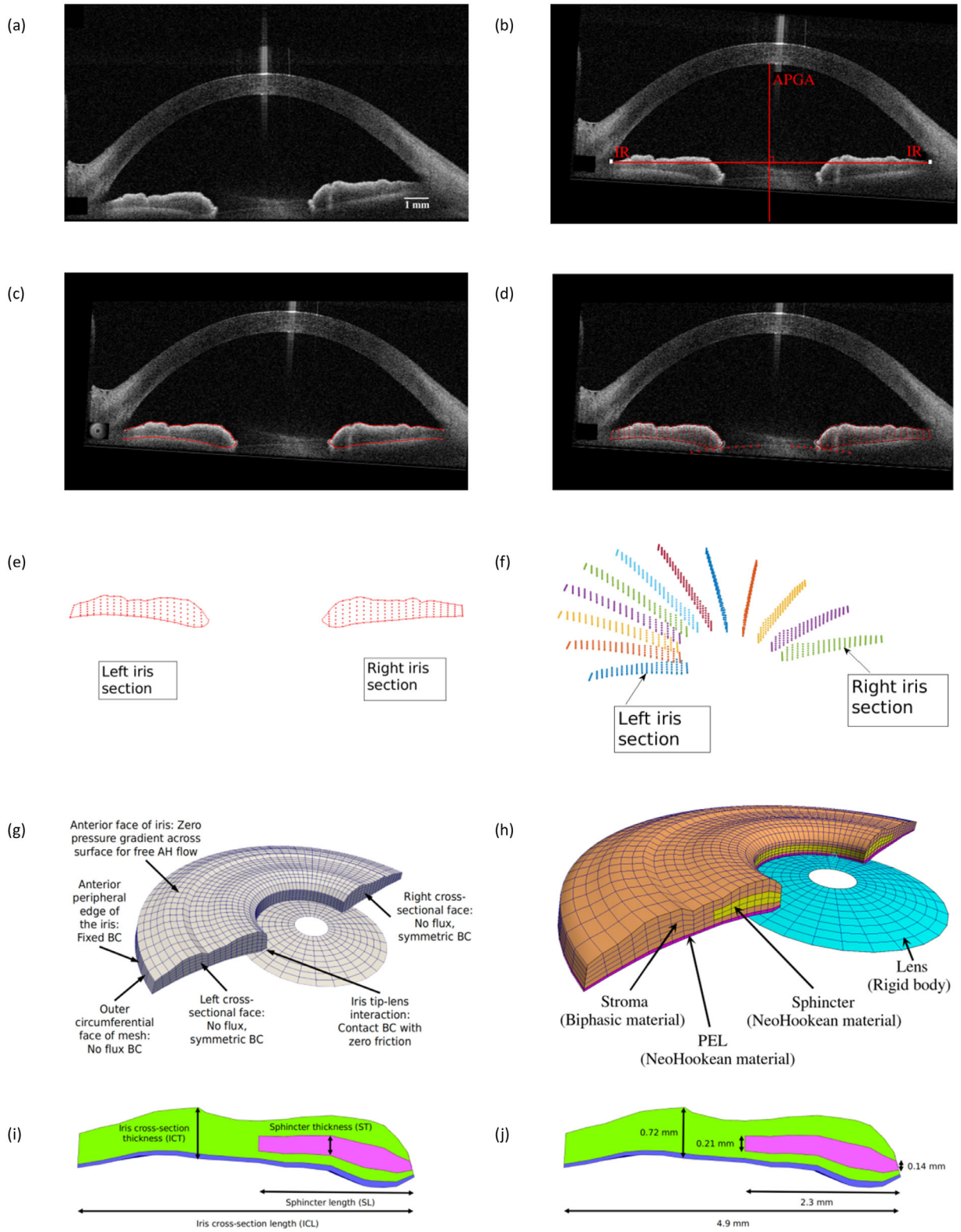

Figure 1. **(a)** An OCT image of the iris and the anterior chamber of the eye. **(b)** Rotated OCT image to align the IR horizontally. The IR and the APGA are shown with *white dots* and with a vertical *red line*, respectively. **(c, d)** The OCT image with left and right iris boundaries marked and discretized into a set of points. **(e)** The left and right iris boundaries extracted from the OCT image. **(f)** The 3D transformation and rotation of the left and right iris boundaries to generate a 3D point cloud. **(g)** A 3D FE mesh of the iris generated from the point cloud with the specified boundary condition for FE simulation. **(h)** Specified tissue layers (i.e., stroma layer in *brown*, pigment epithelial layer in *pink*, and sphincter layer in *yellow*) with the corresponding materials in the iris mesh. **(i, j)** The dimensions of the sphincter and iris used for one of the FE models.

Investigative Ophthalmology & Visual Science

Constitutive Relationships for all Tissue Layers

The iris was assumed to be a heterogeneous structure. Specifically, the sphincter and PEL were considered to be nearly incompressible and to behave as neo-Hookean materials. Their constitutive relationships were defined as:

$$\sigma_{passive} = \frac{2c_1}{J}\left(\tilde{\mathbf{b}} - \frac{1}{3}\tilde{I}_1\mathbf{I}\right) + \frac{K\,ln(J)}{J}\mathbf{I} \quad (1)$$

where σ_{passive} is the passive Cauchy stress tensor, c_1 is the Neo-Hookean material coefficient, $\tilde{I}_1$ is the invariant of the deviatoric part of the right Cauchy-Green deformation tensor defined as $\tilde{\mathbf{C}} = \tilde{\mathbf{F}}^{\mathrm{T}}.\tilde{\mathbf{F}}$, $\mathbf{F}$ is the deformation gradient tensor and $\tilde{\mathbf{F}} = J^{-1/3}\mathbf{F}$, $\tilde{\mathbf{b}}$ is the left Cauchy-Green deformation tensor defined as $\tilde{\mathbf{b}} = \tilde{\mathbf{F}}.\tilde{\mathbf{F}}^{\mathrm{T}}$, J is the Jacobian of the deformation gradient defined as $J = \det(\mathbf{F})$, K is a bulk modulus-like penalty parameter, and $\mathbf{I}$ is the second-order identity tensor. The neo-Hookean material coefficient c_1 is related to the elastic modulus of the material through $E = 4c_1(1 + \nu)$, where ν is the Poisson's ratio (ν was fixed at 0.499 for sphincter and PEL in our simulations).[18]

The sphincter region was assumed to be electrically active, and the active force produced by the smooth muscle cells (SMCs) in the circumferential direction was defined as $\sigma_{\text{active}} = \sigma\, e_\theta \otimes e_\theta$, where σ is the magnitude of the active force and e_θ is the unit circumferential vector. Following previous studies, the magnitude of σ_{active} was assumed to be 40 kPa for both PACG and healthy eyes.[9,16] The total stress in the sphincter region was computed by adding the passive and active components, that is, $\sigma_{\text{total}} = \sigma_{\text{passive}} + \sigma_{\text{active}}$. The AS-OCT video analysis revealed that the iris takes 0.9 to 1.2 seconds for constriction. Therefore we increased the value of the active stress linearly from 0 to 40 kPa in 10 steps with a time discretization of 0.1 second, and at each time step, a static FE simulation was performed.

The stroma of the iris is a sponge-like structure that is composed of 40% water.[19] The aqueous humor (AH) in the anterior chamber is believed to readily flow in and out of the stroma during constriction and dilation of the pupil.[14] Although the cells of the stroma are not compressible, the flow of AH through the tissue boundary makes it compressible.[20] This phenomenon was observed in vivo in previous studies.[21,22] To capture this behavior, the stroma was considered to be a biphasic material consisting of a mixture of a porous-permeable solid and an interstitial fluid. The solid constituent of the mixture was assumed to be compressible with a Poisson's ratio of 0.35,[23] whereas the fluid constituent was treated as incompressible. However, the mixture is compressible because the pores of the solid matrix may gain or lose fluid during the deformation of the mixture. The Cauchy stress for a biphasic material, σ_{biphasic} is given by:

$$\sigma_{biphasic} = -p\mathbf{I} + \sigma_{passive} \quad (2)$$

where p is the interstitial fluid pressure and σ_{passive} is the stress in the solid matrix. We used a compressible neo-Hookean constitutive model to describe the solid matrix of the stroma. The constitutive relation for the hydraulic permeability of the interstitial fluid flowing within the porous solid matrix was defined as:

$$\mathbf{w} = -\mathbf{k} \cdot \nabla(p) \quad (3)$$

where $\mathbf{w}$ is the volumetric flux of the fluid relative to the solid, $\nabla(p)$ is the interstitial fluid pressure gradient, and $\mathbf{k}$ is the is the hydraulic permeability tensor. We also assumed the stroma exhibited a constant isotropic permeability, thus the hydraulic permeability tensor was defined as $\mathbf{k} = k\mathbf{I}$, where k is simply referred as the iris permeability.

Boundary Conditions for all FE Simulations

To recreate the physiological deformation pattern of the iris and associated AH flow during pupil constriction, we applied appropriate different boundary conditions to the FE models (Fig. 1g). For all FE simulations, we fixed the anterior peripheral edge of the iris mesh to mimic its connections with the trabecular meshwork. The nodes on the left/right cross-sectional faces were assigned a symmetric boundary condition, that is, the out-of-plane motion was restricted. We also defined no-flux boundary conditions for the outer circumferential face and the left/right cross-sectional faces of the mesh to prevent AH flow through these faces. However, the AH was allowed to flow through the anterior surface of the iris during constriction. Thus the pressure difference across this surface was set to p = 0 Pa. Note that during pupil constriction, the iris tip slides over the lens surface. To mimic this phenomenon, we defined a sliding-contact boundary condition between the iris tip and the lens surface with a coefficient of friction equal to zero. No external loads were applied to the iris, and its deformations were solely due to the active force produced by the sphincter during contraction. Each FE model was solved using FEBio (3.0, Musculoskeletal Research Laboratories, University of Utah, UT, USA)—a nonlinear FE solver designed for biomechanical studies.[24]

Extraction of Iris Biomechanical Properties

Each iris FE model was characterized by two material parameters, the elastic modulus, c_1, and the permeability, k. To extract these parameters for each iris, we used an inverse FE approach that aimed to match the motion of the iris in the FE simulations to that observed in the OCT images. Specifically, the active force of the sphincter muscle was increased in ten incremental steps, and in each step, the parameters were optimized so that the cross-sectional shape of the iris in the FE simulation best-matched that observed with OCT imaging. For this optimization process, the cost function to be minimized was defined as

$$f(c_1,\ k) = \sum_{n=1}^{10}(1 - IoU_n) \quad (4)$$

where IoU_n is the intersection over the union of iris cross-sections (FE vs. OCT) for a given time step, n. The IoU is a commonly used metric for measuring overlap between two shapes. The IoU is equal to one for two shapes that are perfectly overlapped, and equal to zero when there is no overlap. To obtain the biomechanical properties of each iris, Equation (4) was minimized using the Nelder-Mead algorithm, which is a heuristic search method that can converge to a local minimum.[25] The optimization procedure was therefore repeated multiple times with different initial guesses to ensure global convergence.

A C++ based framework coupled with Unfit (Computational Bioengineering lab, NUS) was developed to

automate the whole process. Unfit is a C++-based nonlinear optimization software suitable for data fitting problems. This framework called the FEBio solver during each iteration of the optimization and then minimized the objective function. Unfit also provided options to define bounds for the variables while using the Nelder-Mead algorithm. We defined physically realistic bounds for the iris of 0.001–50 kPa for c_1 and 0.001–4 mm^2/kPa s for k. We used independent samples *t*-testing to compare the mean stiffness and permeability values between glaucoma and healthy groups. Statistical analyses were performed using the SciPy Python package (SciPy 1.6.0).

To examine the effects of the active stress in the sphincter region on the extracted stiffness and permeability values, we varied the active stress from 20 kPa to 50 kPa in steps of 5 kPa and performed an optimization at each stress level. The optimized stiffness and permeability values were plotted against the applied active stress, and Pearson's correlation (PC) tests were performed. The PC tests provide an output that lies between −1 and 1, where 0 indicates no correlation, and a value below −0.5 or above 0.5 indicates a notable correlation.[26]

Results

The subjects in our study were of Indian/Chinese ethnicity with an average age of 60.2 ± 8.7 for PACG subjects and 57.7 ± 10.1 for healthy subjects.

We found the iris to be stiffer in PACG eyes compared to healthy eyes ($P < 0.001$, Fig. 2a), whereas the permeability was found to be lower ($P = 0.142$, Fig. 2b) in PACG eyes. The elastic moduli of healthy and PACG irides with 40 kPa active stress were 17.1 ± 6.6 kPa and 24.5 ± 8.4 kPa, respectively; whereas the respective permeability values were 0.55 ± 0.2 mm^2/kPa s and 0.41 ± 0.2 mm^2/kPa s. The tissue stiffness was found to increase proportionally with the applied active stress (PC = 0.974, Fig. 2c), whereas the permeability value was uncorrelated with the active stress (PC = −0.193, Fig. 2d).

For all incremental loading steps, our FE simulation results followed the actual iris motion closely (IoU > 0.82 for all eyes). Figure 3 shows the iris deformations for one subject at six different time steps with the "true" iris boundary in red and the FE-simulated iris boundary in blue. Overall, this suggests that our proposed optimization framework

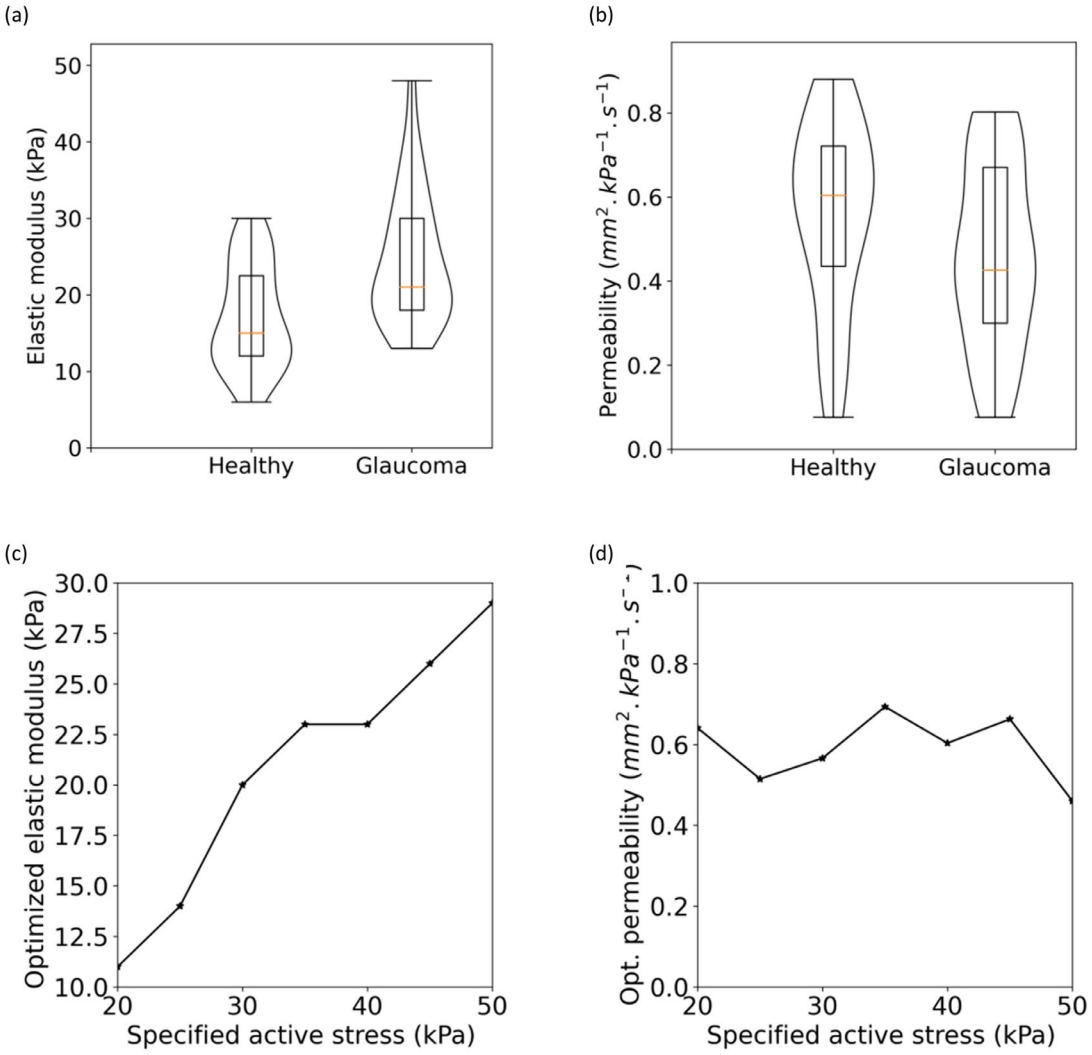

Figure 2. Comparison of **(a)** stiffness and **(b)** permeability values of healthy and PACG irides with 40 kPa of active stress in the sphincter region. **(c, d)** Correlation of tissue stiffness and permeability with the specified active stress.

Investigative Ophthalmology & Visual Science

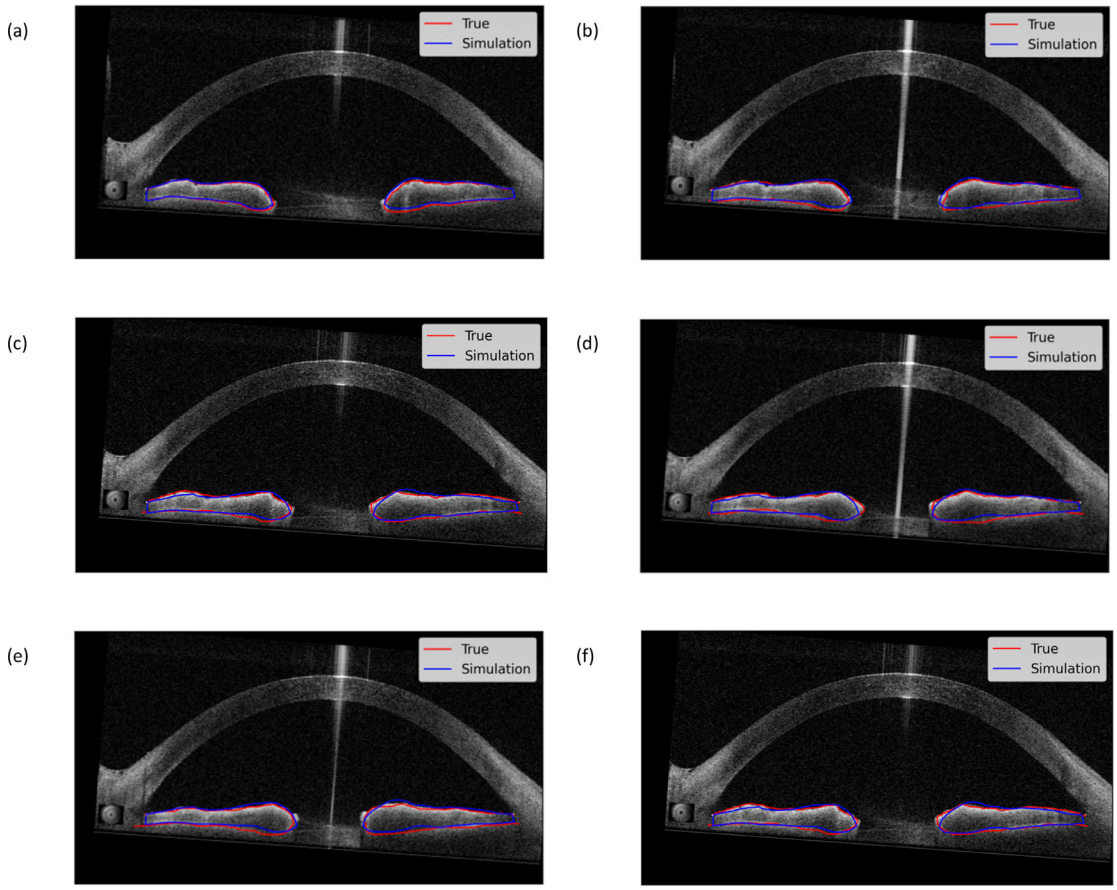

Figure 3. **(a–f)** Deformation of the iris at different instants of time during pupil constriction. The *red lines* are the actual boundaries of the iris, whereas the *blue lines* are the FE simulation results.

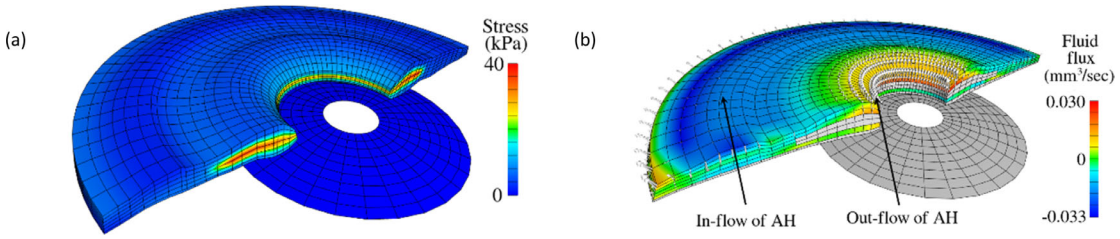

Figure 4. **(a)** Iris mesh in its undeformed reference configuration with the applied active stress in the sphincter region. **(b)** Flow of AH through the stroma at the peak of the constriction.

was successful in matching the observed motion of the iris.

Figure 4a depicts the iris mesh in its initial undeformed configuration in our FE simulation with the specified active stress in the sphincter region. As a consequence of the active stress, the iris mesh deformed. We noted that during iris constriction, the AH flowed into to the iris through the anterior face of the stroma, whereas it flowed out near the iris root and tip (see Fig. 4d). This behavior was consistent across all eyes.

Our FE simulation demonstrated that the iris with a sphincter placed slightly above the posterior surface, so as to align with histology, in the thickness direction produces the most realistic motion during constriction (Fig. 5a). Note that when the sphincter was placed on the posterior side of the iris, the iris tip was found to deflect toward the anterior side (Fig. 5b), whereas with an anteriorly placed sphincter, the iris tip was found to bulge and deflect toward the posterior direction (Fig. 5c).

Our optimization procedure was able to obtain unique solutions for stiffness and permeability (see Fig. 6a). The concave shape of the error space (consistent across all eyes) strongly suggests that the solution is unique. Fig. 6b shows 1) the variation in the error function (see Eq. 4 for the expression of the error/cost function) with stiffness perturbation at the optimal permeability value and 2) the variation in the

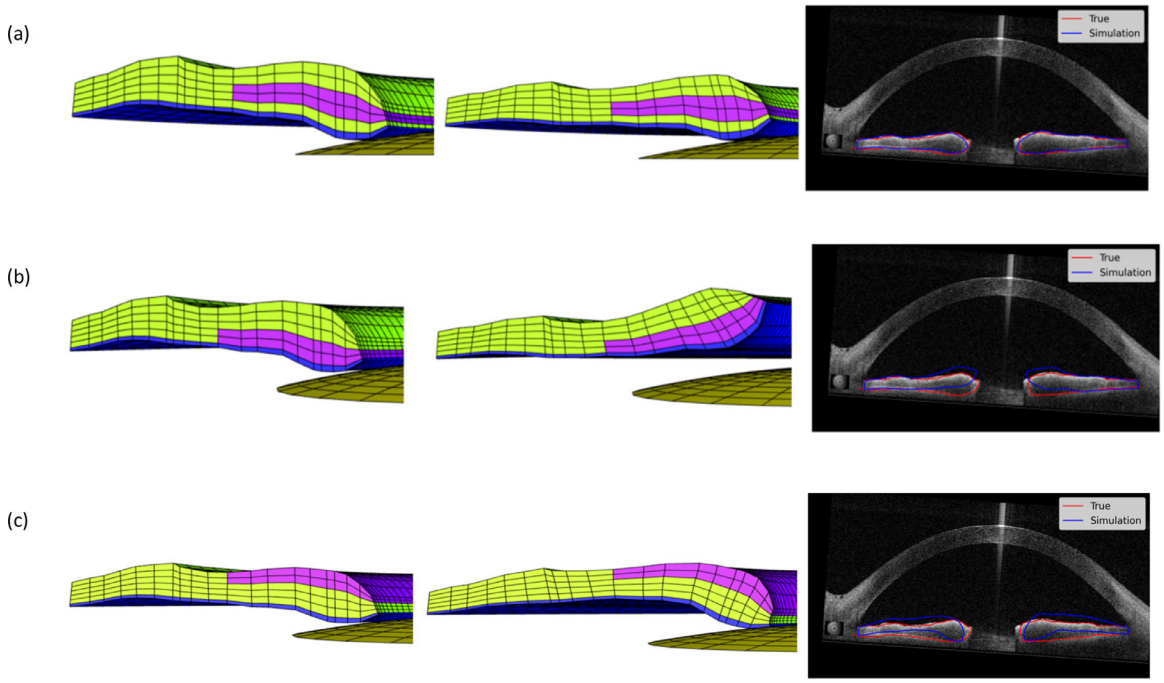

Figure 5. Deformation of the iris during constriction with different locations of the sphincter: placed slightly above the posterior surface **(a)**, posterior side **(b)**, and anterior side **(c)** of the iris. The images on the left and middle show the iris configuration before and after constriction, whereas the images on the right show the FE simulation result with the true iris motion.

error function with permeability perturbation at the optimal stiffness value, respectively.

Discussion

In this study, we used an inverse FE method to evaluate the biomechanical properties of the iris stroma in both PACG and healthy subjects. Our FE model was able to replicate the iris motion observed clinically with OCT imaging during pupil constriction. Through this process we were able to extract the stiffness and permeability of each iris. Overall, we found that in PACG subjects the iris stiffness was higher and permeability lower compared to healthy subjects.

Higher Tissue Stiffness in PACG Subjects

Our study revealed that the iris was stiffer in PACG subjects. This may be explained by the higher density of collagen fibers that has been observed in PACG irides. Indeed, several studies have reported that the density of Type-I collagen in the iris stroma was significantly higher in PACG eyes than in healthy eyes.[4,27] For a given soft tissue, the density of collagen fibers typically correlates with the mechanical stiffness of such a tissue.[28] Using atomic force microscopy, Narayanaswamy et al. compared the elastic moduli of PACG and normal irides and reported values of 2.40 ± 0.82 kPa and 0.85 ± 0.31 kPa, respectively.[8] Pant et al.[9] reported similar observations using an in vivo and noninvasive inverse FE method. Our results are consistent with these observations, but our methodology also had the benefit to additionally assess the permeability of the iris tissue.

The in vivo stiffness of a healthy iris in our study was found to be 17.1 ± 6.6 kPa with 40 kPa of applied active stress. In a recent study, Lee et al.[29] estimated the murine iris stiffness to be 96.1 ± 54.7 kPa following an in vivo protocol. The in vivo iris stiffness of human subjects reported by Pant et al.[9] was 38.8 ± 15.8 kPa with 40 kPa of active stress. Furthermore, in a study by Heys and Barocas,[30] the ex vivo stiffness of bovine iris in the radial direction under uniaxial tensile testing was found to be 27.0 ± 4.0 kPa. Overall, our reported iris stiffness values are consistent and on the same order of magnitude as those reported in the literature, which provides a higher degree of validity to the proposed approach.

It also needs to be noted that the computed stiffness in our study was linearly dependent on the active stress. Because our objective was to recreate the deformation pattern of the iris, we argue that with higher input active stress the tissue stiffness would be higher to keep the deformation at the same level.

Lower Permeability in PACG Patients

In our study, the permeability of the iris was found to be lower in PACG subjects, indicating that water absorption and exudation may be reduced in the irides of PACG subjects during smooth muscle contraction. However, the independent samples *t*-test demonstrated a P value = 0.142, which signifies that the difference in the permeability between healthy and glaucoma groups is not statistically significant at the typically reported level of $P = 0.05$. More patients will need to be recruited to fully understand whether such a trend exists.

The anterior boundary layer and stroma of the iris composed of two principal cell types, that is, fibroblasts and melanocytes. These cells do not form a continuous covering over the anterior iris surface. Therefore AH can permeate freely through the iris stroma. On the other hand, the sphincter is a tissue layer with embedded muscle fibers. These

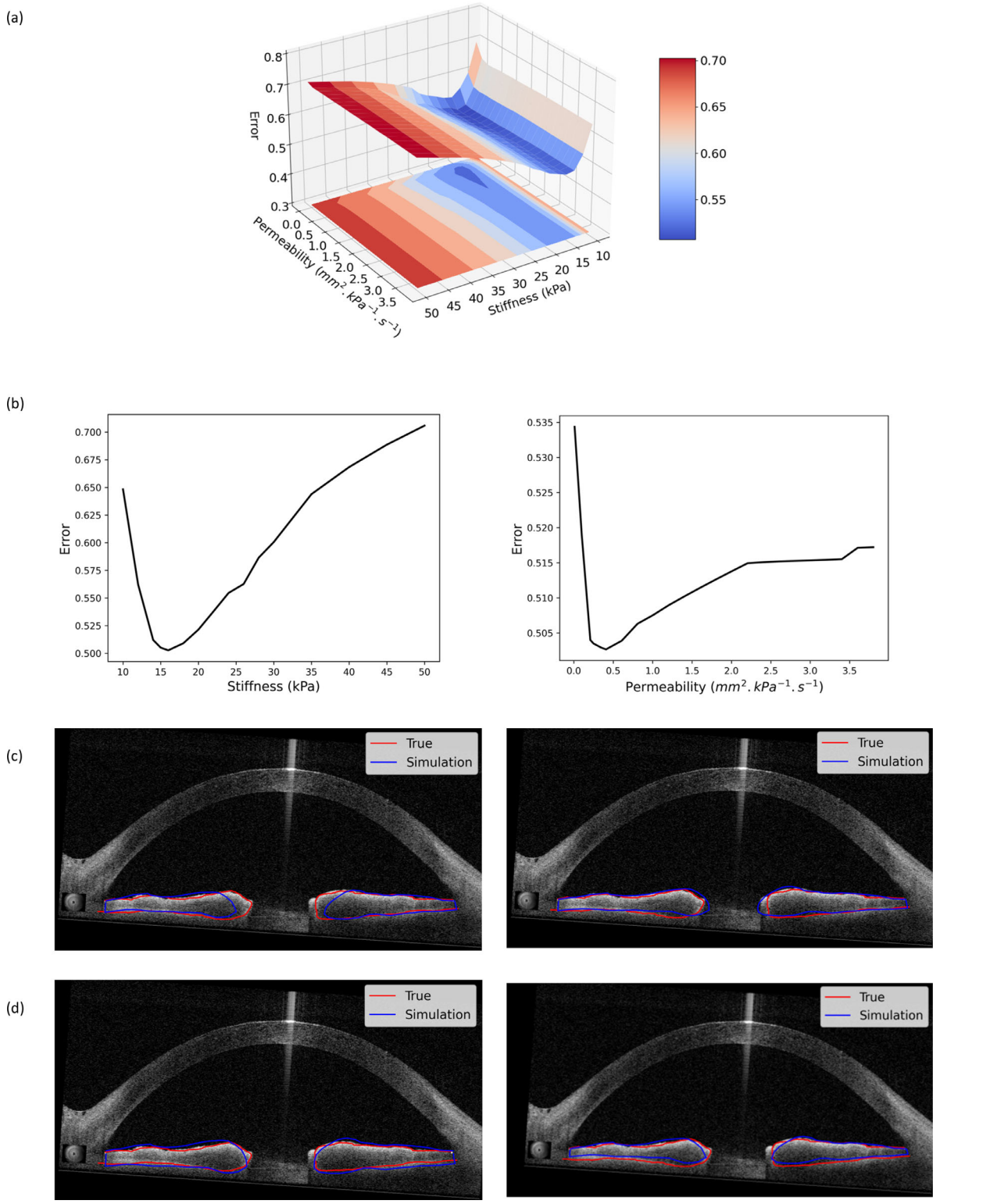

Figure 6. **(a)** The 3D error contour plot (concave shape) strongly suggests that the solution is unique for our proposed fitting methodology. **(b)** *Left:* Variation in the error function with stiffness perturbation at the optimal permeability value. *Right:* Variation in the error function with permeability perturbation at the optimal stiffness value. **(c)** Changes in iris cross-sectional area with variation in stiffness. *Left:* FE simulation result with an elastic modulus of 50 kPa and the true iris deformation after constriction. *Right:* FE simulation result with an elastic modulus of 10 kPa. **(d)** Changes in iris cross-sectional area with variation in permeability. *Left:* FE simulation result with a permeability of 4 mm^2/kPa s. *Right:* FE simulation result with of permeability of 0.01 mm^2/kPa s.

muscle fibers are smooth muscle cells arranged in bundles separated by connective tissue septae that provide conduits for distribution of the autonomic nerve fibers that innervate the muscle.[31] So, we assumed the stroma to be biphasic and the sphincter to be incompressible hyperelastic in our study.

Several studies have reported that the inability of the stroma to lose its interstitial fluid could contribute to the risk of angle-closure.[13,14] Using OCT imaging, Aptel and Denis[32] demonstrated that the volume and cross-sectional area of the iris decreased with pupil dilation. One of the widely accepted reasoning for the change in iris volume is the gain or loss of extracellular water from the spongy iris stroma.[14] Furthermore, angle-closure eyes demonstrate fewer iris crypts compared to eyes with wider angles.[33] It has been hypothesized that irides with a smaller number of crypts are less porous and would therefore allow less AH to flow through. The decrease in permeability in PACG, as reported in our study, suggests that the stromal tissue would not allow the AH to flow rapidly into or out of the tissue during physiological pupil dilation or constriction, and subsequently the iris may not change its volume during the deformation process. This condition could potentially cause the iris to bulge significantly at the periphery and lead to an acute angle-closure attack. However, it is still unclear whether a change in permeability would be a cause or the consequence of glaucoma, and further studies are warranted.

We obtained average iris permeability values of 0.55 ± 0.2 mm^2/kPa s and 0.41 ± 0.2 mm^2/kPa s for healthy and PACG irides, respectively. The high permeability of iris facilitates rapid exchange of fluid during constriction and dilation. In contrast, the human meniscus has a hydraulic permeability of $1.99 \pm 0.79 \times 10^{-6}$ mm^2/kPa s for slow exudation of fluid out of the tissue.[34] In a recent work, Safa et al.[35] reported a permeability value of 3.854×10^{-4} mm^2/kPa s for the porcine optic nerve head. The current literature on iris tissue permeability is limited. In a previous study by our group, we measured the permeability of porcine stroma ex vivo and reported a value of 0.0513 ± 0.02 mm^2/kPa s.[21] Here our optimized permeability values were an order of magnitude higher than theses experimental observations, but this could potentially be explained by differences in methodologies and the fact that ex vivo tissues may not be fully representative of their in vivo state.

In conjunction with the spongy structure filled with AH, the iris also has an abundant vasculature with large arteries, veins, and fine capillaries.[36] The movement of blood in and out of the vasculature structure may also impact the overall tissue behavior. To date, the effect of the vasculature on the biomechanical behavior of the iris during myosis and mydriasis is unknown, and it may require the use of more advanced models (other than biphasic) to fully understand such an impact.

Effects of Stiffness and Permeability on the Deformed Cross-Section of the Iris

We found that both tissue stiffness and permeability affected the iris geometry during constriction. The elastic modulus had a significant contribution, and it mostly controlled the length of the iris during pupil constriction (or pupil size). Figure 6c shows two FE simulations with elastic moduli of 50 kPa and 10 kPa, respectively. With the elastic modulus of 10 kPa, the length of the iris was higher than the true value after constriction, whereas, with 50 kPa, it was smaller (Fig. 6c shows the FE simulation and true iris deformation of a random subject for which the optimized elastic modulus was 16 kPa). On the other hand, tissue permeability was found to control the thickness of the iris during constriction. In our FE simulations, the AH flowed into the iris through the anterior face of the stroma, whereas it flowed out near the iris root and tip. As the inflow surface was larger than the outflow, there would be an accumulation of AH inside the tissue, and subsequently, the iris volume would increase. Figure 6d shows two FE simulations with permeability values of 4 mm^2/kPa s and 0.01 mm^2/kPa s, respectively. It is evident from the results that the iris thickness increased with permeability. With the permeability value of 0.01 mm^2/kPa s, the iris thickness was less than the true value, whereas, with 4 mm^2/kPa s, the thickness was higher (the optimized permeability for this subject was 0.43 mm^2/kPa s). These results signify that both stiffness and permeability control the iris geometry during constriction, and both have distinctive contributions. The error values in the 2D stiffness and permeability space (Fig. 6a) also supported this result as the error value changed with stiffness and permeability in an uncoupled manner. It also explained the noncorrelation of permeability with the applied active stress in the sphincter region (Fig. 2d).

A Framework to Assess Iris Biomechanics In Vivo for Diagnosing PACG

In this study, we have proposed a noninvasive procedure to evaluate the material parameters of the iris in healthy and PACG conditions. This method does not involve any contact procedure, such as tonometry, or any surgical intervention to isolate the tissue. Furthermore, our method can reproduce the actual motion of the iris during various physiological states. As such, it holds promise as a preferred method for tissue characterization.

The characterization of the biomechanical properties of the iris is important as any deviations from homeostasis may indicate a diseased condition.[32] We observed changes in iris stiffness and permeability in PACG subjects which could indicate that these material parameters may be useful markers for early diagnosis.

Limitations

In this study, several limitations warrant further discussion. First, we treated the active stress in the sphincter region as a constant. We did not consider any electrophysiological and electromechanical coupling models for sphincter smooth muscle cells.[37,38] With more advanced models, it may be possible to examine the electrical and chemical response of the iris tissue during miosis and mydriasis. Second, each iris (healthy or PACG) may have its patient-specific activation force. This was not considered for our optimization, but instead, we used an average for all eyes. Our results revealed a strong correlation between the sphincter muscle active stress and the optimized elastic modulus. Therefore, with differences in the activation forces, the elastic moduli may change for healthy and PACG groups, and in such cases, our conclusion that the PACG iris is stiffer than the healthy one may not be valid. Nevertheless, our results still indicate a clear biomechanical difference between the two groups, independent of such an assumption, and also agrees with

Investigative Ophthalmology & Visual Science

literature where stiffness values both for healthy and PACG have been reported.[8,9] There is no literature available that compares the sphincter muscle active force in healthy and PACG conditions. In the future, we will aim to better estimate these patient-specific forces in healthy and PACG conditions. Third, we only used a single OCT B-Scan (horizontal plane) to reconstruct the 3D geometry of the iris during constriction. Using multiple B-scans in the circumferential direction may yield better results; however, such an approach is not yet feasible as one would have to image the 3D iris in real-time as it deforms during constriction with a high acquisition rate. This may be possible with next-generation OCT devices. Fourth, all tissues (stroma, PEL, sphincter) were described with a simple isotropic Neo-Hookean formulation. Although the active stress in the sphincter region was applied in the circumferential direction, we did not define any circumferential fibers. The rationale behind this was to keep the number of unknown parameters low so that we could avoid the "non-uniqueness problem" that is common in many biomechanical applications. Fifth, all tissues were assumed to be hyperelastic because of their large deformations but not viscoelastic. Several studies have suggested that the iris tissue exhibits viscoelastic properties.[17,39,40] Therefore, iris material parameters should be time- and rate-dependent, and the iris should exhibit higher stiffness at higher rates of deformation. The study of Bergamin et al.[41] revealed that the latency and the contraction time of the pupil during constriction were 0.52 seconds and 0.4 seconds, respectively, whereas in our study, the OCT image analysis showed that the constriction time of the pupil to be 0.9 to 1.2 seconds. Also, because miosis and mydriasis occur rapidly at a rate of approximately 4 mm/s,[42] a viscoelastic model may be suitable to describe iris biomechanics, and this could be considered in future studies. Sixth, we did not consider the residual stresses that could be present in the iris.[43] Residual stresses can influence the local biomechanical behavior by reducing stress concentrations.[17] Seventh, the lens was considered as a rigid body, and all its degrees-of-freedom were restricted. Because accommodation reflex can cause myosis/mydriasis-like behavior, our study in its current form cannot model this behavior. Finally, we optimized the material parameters for pupil constriction, and thus, in our simulation, only the sphincter region was active. In the future, we aim to evaluate iris biomechanics while considering both the dilation and constriction of the pupil.

Conclusion

Our study used an inverse FE approach to assess the in vivo stiffness and permeability of the iris directly from OCT imaging during pupil constriction. We found that PACG eyes exhibited higher iris stiffness but lower permeability. If these tools were to be translated clinically, they could aid in the diagnosis of PACG.

Acknowledgments

Supported by the Singapore Ministry of Education Academic Research Funds Tier 1 (R-397-000-294-114 (MJAG)), the Singapore Ministry of Education Tier 2 (R-397-000-280-112, R-397-000-308-112 (MJAG)), and the National Medical Research Council (Grant NMRC/STAR/ 0023/ 2014 (TA)).

Disclosure: **S.K. Panda,** None; **R.K.Y. Tan,** None; **T.A. Tun,** None; **M.L. Buist,** None; **M. Nongpiur,** None; **M. Baskaran,** None; **T. Aung,** None; **M.J.A. Girard,** None

References

1. Chan EW, Li X, Tham Y-C, Liao J, Wong TY, Aung T, Cheng C-Y. Glaucoma in asia: regional prevalence variations and future projections. *Br J Ophthalmol*. 2016;100:78–85.
2. Friedman DS, He M. Anterior chamber angle assessment techniques. *Surv Ophthalmol*. 2008;53:250–273.
3. Lee Y, Sung KR, Na JH, Sun JH. Dynamic changes in anterior segment (as) parameters in eyes with primary angle closure (pac) and pac glaucoma and open-angle eyes assessed using as optical coherence tomography. *Invest Ophthalmol Vis Sci*. 2012;53:693–697.
4. He M, Lu Y, Liu X, Ye T, Foster PJ. Histologic changes of the iris in the development of angle closure in chinese eyes. *J Glaucoma*. 2008;17:386–392.
5. Congdon NG, Youlin Q, Quigley H, et al. Biometry and primary angle-closure glaucoma among chinese, white, and black populations. *Ophthalmology*. 1997;104:1489–1495.
6. Wilensky JT, Kaufman PL, Frohlichstein D, et al. Follow-up of angle-closure glaucoma suspects. *Am J Ophthalmol*. 1993;115:338–346.
7. Friedman DS, Gazzard G, Foster P, et al. Ultrasonographic biomicroscopy, scheimpflug photography, and novel provocative tests in contralateral eyes of chinese patients initially seen with acute angle closure. *Arcb Ophthalmol*. 2003;121:633–642.
8. Narayanaswamy A, Nai MH, Nongpiur ME, et al. Young's modulus determination of normal and glaucomatous human iris. *Invest Ophthalmol Vis Sci*. 2019;60:2690–2695.
9. Pant AD, Gogte P, Pathak-Ray V, Dorairaj SK, Amini R. Increased iris stiffness in patients with a history of angle-closure glaucoma: an image-based inverse modeling analysis. *Invest Ophthalmol Vis Sci*. 2018;59:4134–4142.
10. Gregersen E. On the imbibition of the human iris stroma with the aqueous humour: summary of thesis. *Acta Ophthalmologica*. 1961;39(4):623–625.
11. Chua J, Thakku SG, Tun TA, et al. Iris crypts influence dynamic changes of iris volume. *Ophthalmology*. 2016;123:2077–2084.
12. Chua J, Thakku SG, Pham TH, et al. Automated detection of iris furrows and their influence on dynamic iris volume change. *Sci Rep*. 2017;7:1–8.
13. Quigley HA, Silver DM, Friedman DS, et al. Iris cross-sectional area decreases with pupil dilation and its dynamic behavior is a risk factor in angle closure. *J Glaucoma*. 2009;18:173–179.
14. Quigley HA. The iris is a sponge: a cause of angle closure. *Ophthalmology*. 2010;117:1–2.
15. Zheng C, Guzman CP, Cheung CY, et al. Analysis of anterior segment dynamics using anterior segment optical coherence tomography before and after laser peripheral iridotomy. *JAMA Ophthalmol*. 2013;131:44–49.
16. Amini R, Whitcomb JE, Al-Qaisi MK, et al. The posterior location of the dilator muscle induces anterior iris bowing during dilation, even in the absence of pupillary block. *Invest Ophthalmol Vis Sci*. 2012;53:1188–1194.
17. Whitcomb JE, Amini R, Simha NK, Barocas VH. Anterior–posterior asymmetry in iris mechanics measured by indentation. *Exp Eye Res*. 2011;93:475–481.
18. Panda SK, Buist ML. A finite element approach for gastrointestinal tissue mechanics. *Int J Numer Methods Biomed Eng*. 2019;35(12):e3269.
19. Tan RK, Wang X, Chan AS, et al. Permeability of the porcine iris stroma. *Exp Eye Res*. 2019;181:190–196.
20. Tan RK, Wang X, Perera SA, Girard MJ. Numerical stress analysis of the iris tissue induced by pupil expansion: Comparison of commercial devices. *PLoS One*. 2018;13(3):e0194141.

21. Mak H, Xu G, Leung CK-S. Imaging the iris with swept-source optical coherence tomography: relationship between iris volume and primary angle closure. *Ophthalmology*. 2013;120:2517–2524.
22. Tun TA, Baskaran M, Perera SA, et al. Sectoral variations of iridocorneal angle width and iris volume in chinese singaporeans: a swept-source optical coherence tomography study. *Graefes Arch Clin Exp Ophthalmol*. 2014;252:1127–1132.
23. Pant AD, Dorairaj SK, Amini R. Appropriate objective functions for quantifying iris mechanical properties using inverse finite element modeling. *J Biomech Eng*. 2018;140(7):074502-1–074502-6.
24. Maas SA, Ellis BJ, Ateshian GA, Weiss JA. Febio: Finite elements for biomechanics. *J Biomech Eng*. 2012;134(1):011005.
25. McKinnon KI. Convergence of the Nelder–Mead Simplex method to a nonstationary point. *SIAM J Optim*. 1998;9(1):148–158.
26. Benesty J, Chen J, Huang Y, Cohen I. Pearson correlation coefficient. In: Cohen I, Huang Y, Chen J, Benesty J, eds. *Noise reduction in speech processing*. Berlin: Springer, 2009:1–4.
27. Seet L-F, Narayanaswamy A, Finger SN, et al. Distinct iris gene expression profiles of primary angle closure glaucoma and primary open angle glaucoma and their interaction with ocular biometric parameters. *Clin Exp Ophthalmol*. 2016;44(8):684–692.
28. Swift J, Ivanovska IL, Buxboim A, et al. Nuclear lamin–A scales with tissue stiffness and enhances matrix-directed differentiation. *Science*. 2013;341(6149):1240104.
29. Lee C, Li G, Stamer WD, Ethier CR. In vivo estimation of murine iris stiffness using finite element modeling. *Exp Eye Res*. 2021;202:108374.
30. Heys J, Barocas V. Mechanical characterization of the bovine iris. *J Biomech*. 1999;32(9):999–1003.
31. Freddo TF. Ultrastructure of the iris. *Microsc Res Tech*. 1996;33(5):369–389.
32. Aptel F, Denis P. Optical coherence tomography quantitative analysis of iris volume changes after pharmacologic mydriasis. *Ophthalmology*. 2010;117:3–10.
33. Sidhartha E, Nongpiur ME, Cheung CY, et al. Relationship between iris surface features and angle width in asian eyes. *Invest Ophthalmol Vis Sci*. 2014;55:8144–8148.
34. Joshi MD, Suh JK, Marui T, Woo SLY. Interspecies variation of compressive biomechanical properties of the meniscus. *J Biomed Mater Res*. 1995;29:823–828.
35. Safa BN, Read AT, Ethier CR. Assessment of the viscoelastic mechanical properties of the porcine optic nerve head using micromechanical testing and finite element modeling. *bioRxiv*, 2021.
36. Song Y, Song YJ, Ko MK. A study of the vascular network of the iris using flat preparation. *Korean J Ophthalmol*. 2009;23:296–300.
37. Imaizumi Y, Furuichi Y, Watanabe M. Electrical properties of iris sphincter. Daniel EE, Tsuchida S, Watanabe M, Tomita T, eds. *Sphincters: Normal Function Changes in Disease*. Boca Raton, FL: CRC Press; 1995:401.
38. Panda SK, Buist ML. An active finite viscoelastic model for gastric smooth muscle contraction. *bioRxiv*, 2021, doi:https://doi.org/10.1101/2021.01.26.428273
39. Panda SK, Buist ML. A finite nonlinear hyper-viscoelastic model for soft biological tissues. *J Biomechan*. 2018;69:121–128.
40. Panda SK, Buist ML. A viscoelastic framework for inflation testing of gastrointestinal tissue. *J Mech Behav Biomed Mater*. 2020;103:103569.
41. Bergamin O, Schoetzau A, Sugimoto K, Zulauf M. The influence of iris color on the pupillary light reflex. *Graefes Arch Clin Exp Ophthalmol*. 1998;236:567–570.
42. Morgan SS, Hollenhorst RW, Ogle KN. Speed of pupillary light response following topical pilocarpine or tropicamide. *Am J Ophthalmol*. 1968;66:835–844.
43. Wang R, Raykin J, Gleason RL, Jr, Ethier CR. Residual deformations in ocular tissues. *J R Soc Interface*. 2015;12(105):20141101.

Investigative Ophthalmology & Visual Science